Applied Surface Science 686 (2025) 161967

Contents lists available at ScienceDirect

Applied Surface Science

journal homepage: www.elsevier.com/locate/apsusc

Full Length Article

Tuning spike-like morphologies in Silicon by sustainable fs-laser processing in air for enhanced light absorption

Gonzalo Gomez-Munoz [a,*], Rafael Benítez-Fernández [b], Guillermo Godoy-Perez [b], Fatima Cabello [a], Marina Garcia-Pardo [a], Daniel Caudevilla [b], Jose Gonzalo [a], Javier Solis [a], Mario Garcia-Lechuga [a], Javier Olea [b], David Pastor [b], Jan Siegel [a,*]

[a] Laser Processing Group, Instituto de Óptica "Daza de Valdés" (IO), CSIC, Serrano 121, 28006 Madrid, Spain
[b] Departamento de Estructura de la Materia, Física Térmica y Electrónica, Facultad de Ciencias Físicas, UCM, 28040 Madrid, Spain

ARTICLE INFO

Keywords:
femtosecond laser processing
silicon
black silicon
spiky silicon
processing in air
laser induced periodic surface structures (LIPSS)

ABSTRACT

In this work, we demonstrate that ultrafast laser processing (1030 nm, 290 fs) of silicon in ambient air strongly improves the material's performance in terms of absorption, both in the visible and near infrared spectral range, which paves the way for further studies on increasing the sub-bandgap absorption after texturing, suggesting the material developed as a sustainable substitute for black silicon processed in greenhouse gases atmospheres. Our approach is based on the fabrication of spike-like morphologies in ambient air and the subsequent annealing of the material by pulsed laser melting or rapid thermal annealing to recover its crystalline phase. In particular, the influence of three main processing parameters (fluence, pulse number and repetition rate) on the properties of the spike-like structures has been investigated, each of them revealing the possibility of a direct control on the size, shape and period of the spikes, and achieving a total tuning range of the period from 4 μm to 14 μm for a single laser wavelength. Macroscopic areas have been fabricated using short processing times, yielding absorption values $A > 94\%$ over the UV–VIS-NIR spectral range (250 nm - 1100 nm) without hyperdoping, and $A \geq 20\%$ for longer wavelengths up to 2500 nm, while preserving the electrical performance of pristine silicon.

1. Introduction:

Laser processing is a powerful tool for functionalizing the surface of a wide range of materials. By controlling the topography of a material surface through nano- and microtexturing, for instance, it is possible to engineer the functionalities of certain material systems, allowing their implementation and use for applications in numerous fields, such as structural coloration, wettability or biomedicine [1,2].

As demonstrated in previous studies [2,3], one highly efficient laser-texturing method is based on the formation of Laser Induced Periodic Surface Structures (LIPSS) with ultrafast laser pulses. Here, the interference of the incident light with a scattered or excited surface wave leads to a modulated intensity distribution that is imprinted into the material, giving rise to the simultaneous formation of multiple nano– or micrometer–sized surface structures [3–5]. The underlying self-organization process leads to different morphologies, depending on the processing conditions (ripples [6], grooves [7], spikes [8], 'cauliflower' structures [9]…). At moderate fluences, LIPSS can manifest as ripple-like morphologies aligned perpendicular to or along the polarization vector of the incident light [3–5], depending on the material. The resulting topography for a given material also depends on the irradiation parameters, such as pulse length, laser fluence, number of effective pulses used, surface roughness or ambient gas [1,5–7,10,11]. For high fluences and elevated pulse numbers, grooves and spike-like structures are formed, which is commonly attributed to an interplay between surface plasmon excitation and hydrodynamics of the molten material as underlying formation mechanisms [12]. LIPSS-based processing has proven to be an appropriate technique to texture material surfaces for a variety of functionalities, enabling their use in photovoltaic (PV) applications [10,13–16] or surface wetting applications [11], among others [1,2,17].

Despite these achievements, for the particular case of Silicon (Si), a rather poor crystallinity and high defect density are typically observed after processing due to both pressure waves generated in reaction to the ablation pressure of material ejected from the surface and fast quench rates of the molten material [18–21]. This lack in crystallinity, together

* Corresponding authors.
E-mail addresses: gonzalo.gomez@io.cfmac.csic.es (G. Gomez-Munoz), j.siegel@io.cfmac.csic.es (J. Siegel).

https://doi.org/10.1016/j.apsusc.2024.161967
Received 18 July 2024; Received in revised form 21 November 2024; Accepted 28 November 2024
Available online 29 November 2024

with the defects introduced by the fs-processing, limits the optoelectronic performance of Si because of the carrier's lifetime reduction that it triggers [22]. Thus, as improving light absorption for Si applications is the ultimate goal, the processed material must be treated in order to recover the lost crystallinity and eliminate defects in order to recover or even improve the electrical behaviour of the material. Different annealing techniques can be applied for this purpose [15,19,22–24].

One of the main factors that limits Silicon's performance efficiency in optoelectronic and PV applications is its high reflectivity, strongly reducing light absorption. The latter does not exceed 65% in the visible (VIS) and near infrared (NIR) spectral regions (respectively, from 400 to 750 nm for VIS and from 750 to 1100 nm for NIR) and is negligible for wavelengths $>$ 1.1 μm. Surface texturing to achieve a spike-like morphology with high aspect ratios has been proposed as a means to increase light absorption via multiple reflections of incident photons [13–15,25–27]. In this way, very low reflectivity values can be achieved, providing the material with a black appearance upon certain illumination angles, which is why it is often referred to as "black silicon" (BSi). This behaviour leads to an enhanced light absorption in the VIS-NIR region, improving Si performance in energy harvesting [15,26,27], photodetection [16,28] and other photovoltaic and optoelectronic applications.

While the above-mentioned texturing strategy shows promise for the VIS-NIR spectral region, additional strategies are required to increase the low absorption for longer wavelengths. To this end, material hyperdoping has been proposed, which can be achieved via fs-laser processing in an SF_6 atmosphere, leading to the incorporation of sulphur (S) atoms which increases the absorption for longer wavelengths via deep centre formation [15,29,30]. Also, in this case of dopant incorporation, the processed material features sharp spikes that support the multiple reflection mechanism [10,15,29,31–35]. Yet it needs to be emphasized that SF_6 is a greenhouse gas (GhG) and should therefore be avoided due to its harmful effect on nature. There are several works of laser processing of Si in other gases at different pressures (Cl_2 [29,31], N_2 [31], NF_3 [23], ambient air [31,36,37], vacuum [33]…) or in even liquids [28]. Many of them explore the influence of the gas pressure on the morphology, since the expansion dynamics of the ejected molten material is strongly influenced by it [38,39], while others investigate if gas atoms are incorporated into the silicon surface [20,23,31,40], for instance to act as dopants for absorption in the medium infrared (MIR) region (from 1100 nm to 3000 nm), as demonstrated for the above-mentioned case of SF_6. Noteworthy, non-gas based hyperdoping strategies have been reported [16,41].

In this work we have studied the influence of the fs-irradiation parameters on the properties of laser-textured Si fabricated in air, developing a fast, scalable, cost-effective and green method for manufacturing reproducible and tunable spike-like silicon (SSi) textures in monocrystalline Si(100) samples. We have conducted a parametric study focusing on three main processing parameters: the incident laser fluence, the number of effective pulses and the laser repetition rate, achieving tunability of the shape and size of the induced morphologies from dome-like ($\Lambda_{MIN} \sim 4$ μm) to spike-like microstructures ($\Lambda_{MAX} \sim 14$ μm). A detailed analysis of the impact of these three parameters on the absorption enhancement due to multiple reflections and light trapping is given. Additionally, Pulsed Laser Annealing (PLA) and Rapid Thermal Annealing (RTA) have been performed on the textured samples in order to recover the crystallinity lost during fs-processing, which is crucial for photovoltaic applications. After annealing, the optimized structures showed electrical properties as good as those of the original bare, crystalline Si. The morphology, optical properties and crystalline information of the samples have been characterized by Optical Microscopy (OM), Scanning Electron Microscopy (SEM), Spectrophotometry and Raman Spectroscopy (RS). The composition and electrical properties in this study have been determined by Energy Dispersive X-ray microanalysis (EDX) and sheet resistance and Hall effect measurements.

2. Experimental

Commercial 2", double-side polished, boron-doped, p-type Si(100) wafers with 500 μm thickness and a maximum electrical resistivity of 10 Ω·cm have been laser-processed in ambient air conditions. Close to the sample front surface, a tube for air suction is installed in order to remove the dense fume that is produced during laser irradiation. The laser source used is an Yb-doped fiber laser (Satsuma HP, Amplitude Systemes) operating at a central wavelength of 1030 nm, with a pulse duration of 290 fs and a maximum pulse repetition rate of 500 kHz that can be varied within the 1-500 kHz interval. The beam is steered through a system composed of a galvanometric mirror scanner (ScanCube 14, Scanlab) and a F-theta lens (f = 254 mm), which scans the laser focus over the stationary wafer surface. The F-theta lens provides a flat-field focusing over an area of 7×7 cm^2. In order to further reduce a possible interaction between the incident beam and the fume expelled from the material surface in a slight upward direction, beam scanning is performed along the horizontal direction and from the top of the wafer to the bottom. The laser beam polarization was linear and controlled by the use of a λ/2 waveplate to be vertical on the sample, perpendicular to the scanning direction. The spot diameter at the sample surface of the Gaussian-shaped laser beam was determined following the method proposed by Liu to be $2\omega_0 = 46$ μm ($1/e^2$ intensity) [42], where ω_0 is the spot radius.

The processing strategy consisted in the fabrication of homogeneously irradiated areas and exploring three main processing parameters: the peak fluence (F) incident on the sample surface, the effective number of pulses (N_{eff}) and the laser repetition rate (f_{rep}). Each of these parameters is investigated in an independent study, so that altering just one parameter and keeping constant the other two, the influence of the modified factor can be established, aimed at identifying optimized parameters for obtaining spike-like Si (SSi) with high absorptivity. Additionally, some static multi-pulse irradiations have been performed to achieve a better understanding of the effect of the number of pulses in the spikes formation. Except f_{rep}, both F and N_{eff} cannot be set directly in the laser-control software; these are calculated from other control parameters as follows (1,2):

$$F = \frac{2E}{\pi \cdot \omega_0^2} \tag{1}$$

$$N_{eff} = \frac{\pi \cdot \omega_0^2 \cdot f_{rep}}{v_s \cdot d} \tag{2}$$

In Eqs. (1) and (2) E is the energy per pulse (calculated from the total emitted power and the repetition rate), v_s is the scanning speed and d is the separation between consecutive scan lines, fixed as a constant for all irradiations (d = 7.5 μm). Note that a desired N_{eff} value can be obtained for different repletion rates by changing the scanning speed. The scanner is operated by a software (LaserDESK, Scanlab) that allows to modify these three parameters in both, static and scanning irradiation.

After processing, extensive optical characterization was performed on the fabricated structures. For the specific case of statically irradiated samples, the optical transmission at 1064 nm was measured by focusing a low power cw laser at the spot center and measuring the transmitted power. In addition, all samples were characterized by OM with λ = 460 nm LED illumination. A Fast Fourier Transform (FFT) has been performed on the top-view images recorded with OM in order to evaluate the presence of periodic structures and quantify their respective periods.

To this end, radial averaging has been performed on the FFTs in order to determine the more intense spatial frequency (see Supplementary Figure S1), corresponding to the most frequent periodicity (mode, in statistical terms) of the generated structure. This value is referred to throughout the manuscript as the period, Λ, and it is represented in figures as points. The analysis of the individual FFTs also include the retrieval of highest and lowest spatial frequencies (see

Supplementary Figure S1), defining the periodicity range, $\Delta\Lambda$, observed on the generated structure. This value is represented in figures with shaded areas.

The morphology of the processed samples has also been assessed by SEM in secondary electron detection mode (SE). Two different electron microscopes have been used: a JEOL 7600F JSM SEM for recording top-view images of the processed areas and, in order to better appreciate the conical structures of the texture, and a Hitachi S-8000 SEM for angled incidence (45°) observation. The composition of the samples was estimated by EDX microanalysis in a JEOL 6400J JSM SEM using an INCA EDX system operated with an acceleration voltage of $20\,kV$. The total (specular and diffuse) reflectivity (R) and transmission (T) of the samples were measured by Spectrophotometry with a Cary 5000 spectrophotometer and a Perkin Elmer Lambda 1050+ UV/Vis/NIR spectrophotometer together with a 150 mm integrating sphere for the reflectance measurements. The integrating sphere counts with a photomultiplier (for the 200-850 nm range) and with an InGaAs photodetector (for the 850-2500 nm range). Its absorptance (A) was calculated as expressed in (3).

$$A = 1 - (T + R) \tag{3}$$

Then, the areas with the highest absorption values (assessed by Spectrophotometry) were reproduced and subjected to two different annealing treatments: PLA and RTA. PLA processing was performed in air, irradiating the fs-laser processed regions with an ArF excimer laser ($\lambda = 193$ nm, 20 ns full width half maximum). The PLA irradiation setup consisted of a diffractive beam shaper (HOLO-OR) combined with a fused silica plano-convex lens (focal length 85.4 mm at 193 nm). This system allowed precisely imaging the incident excimer laser beam to lead to a top-hat laser beam profile at the working plane where the sample surface was placed. The irradiation spot had a square shape with a size of 2.56×2.56 mm^2 with sharp edges and a uniform-intensity better than 5%. The sample was moved between individual pulses by a step that equals the spot dimension in order to process the entire of the fs-processed area (11×11 mm^2), using a single laser pulse in each step. The overlapping between consecutive horizontal and vertical irradiated areas was 10 μm. To determine the best irradiation conditions for recovering the crystallinity of the processed SSi areas, we processed different areas at increasing energy densities of the ArF excimer laser pulse, F_{PLA}, in the 1.3 to 2.0 J/cm^2 range. The energy density uncertainty was estimated to be 10%. RTA processing is carried out using a commercial rapid thermal processing system with multi-gas capabilities (MPTC RTP 600 model). The conditions applied are: temperature up to 1000 °C for 2 minutes in an Ar atmosphere.

In order to study the crystallinity of the fs-processed samples, as well as of the annealed samples, Raman spectra were acquired using a scatter confocal micro-Raman NT-MDT NTegra Spectra equipped with a coupled charge detector cooled with liquid nitrogen. The scattered light was recorded at room temperature in unpolarized backscattering configuration using the $\lambda = 532$ nm laser wavelength. The visible Raman spectra were obtained using a confocal micro-Raman system with a ×20 objective and typical spot of ~1 μm and a spectral slitwidth of 0.9 cm^{-1}. Considering the absorption coefficient of crystalline Si at the wavelength used [43], we estimate a probing depth of around 800 nm.

The electrical transport characterization of the samples was performed in the van der Pauw configuration at room temperature (RT) by means of sheet resistance and Hall measurements. A Keithley SCS 4200 system, equipped with four Source and Measure Units, was used for these measurements. The samples consisted of 1×1 cm^2 samples, each performing four Ti/Al (100/200 nm) e-beam deposited electrodes at the corners. A magnetic field of 0.9 T was applied during the Hall effect measurements. All the measurements were performed in the four possible van der Pauw configurations. For each configuration, both the polarity of the current source and the direction of the magnetic field were alternated (yielding a total of 16 measurements), to minimize spurious thermo-galvanomagnetic effects.

3. Results and discussion:

The first parameter explored in the study has been the pulse peak fluence F, processing at a constant repetition rate $f_{rep} = 50$ kHz and number of pulses $N_{eff} = 200$ pulses, covering a range from $F = 0.2$ J/cm^2 to 1.8 J/cm^2. For the lowest fluence (0.2 J/cm^2), parallel ripple-like structures with orientation perpendicular to the laser polarization were formed, corresponding to the so-called low spatial frequency LIPSS [12], featuring a period, Λ, around $\Lambda = 790$ nm (see Supplementary Figure S2). Between 0.4-0.8 J/cm^2, the surface showed a much-increased roughness with feature sizes of approximately 1 μm (see Supplementary Figure S3). OM images of the surfaces processed at fluence values between 0.8 J/cm^2 and 1.8 J/cm^2 are displayed in Figure 1 (a–f). It can be seen that for all areas with $F \geq 1.0$ J/cm^2, randomly-oriented structures with circular appearance are obtained. Moreover, a strong fluence dependence on the diameter and period of the structures is evident, which is consistent with the results observed in Si processed in SF_6 atmosphere reported by the Mazur group [10,15,29,38].

The insets in Figure 1(a–f) correspond to the FFT of the images, revealing a ring structure whose diameter decreases with fluence. The presence of such a ring structure in the FFTs demonstrates the presence of periodic features with no preferred orientation. It must be considered that, due to the 3D nature of the formed structures, the short depth of field of the OM with respect to the height of the structure leaves room for differences in exact imaging plane for the different fluences. While this would lead to differences in the apparent diameter of the structure (not analysed here), it will not influence their lateral position and periodicity. We have analyzed the FFT images according to the procedure described in Section 2 and the result of the so-determined period of the structures is displayed as a function of fluence in Figure 1(g). Despite the width of the periodicity range ($\Delta\Lambda$, represented as a shaded area in Figure 1(g)), an increasing tendency of the period with fluence can be observed, consistent with the direct observation of the images in Figure 1(a–f). The period value increases from $\Lambda = 3.9$ μm under a peak fluence irradiation of 1.0 J/cm^2 to $\Lambda = 6.1$ μm for 1.6 J/cm^2. Structures with periods that lie within this range have been reported upon irradiation of Si in SF_6 atmosphere, using a Gaussian intensity profile without beam scanning, and thus processing a very small region [44]. In contrast, the strategy proposed here to fabricate large areas via beam scanning allows for a statistically more representative analysis by averaging over numerous structures formed.

According to calculations [45], an increase of the height and the diameter of the cones would lead to a reduction in reflectivity in case that the base diameter of the conical structures is smaller than 1.3 times the period. This suggests that for our case, an optimum structure in terms of low reflectivity should consist of closely packed, adjoining cones with elevated heights. In this context, the results of Peng et al. should be mentioned, who found that the average spike height is not a linear function of pulse energy but increases first and then decreases [33].

In order to study the influence of N_{eff} on the structure features, we have used the same f_{rep} as in the previous study (50 kHz). Even though the diameter of the structures for 1.6 J/cm^2 and 1.8 J/cm^2 (Figure 1 (e–f)) were larger, the expelled material for these very high fluences led to a strong collateral wafer contamination and fume formation which may affect subsequent irradiations [33]. Therefore, we have fixed for the study the next highest fluence value (1.4 J/cm^2, related to a structure period $\Lambda = 5.4$ μm). The results for this N_{eff}-dependence study are shown in Figure 2. As observed for the F-dependence study, there is also a threshold value (here for the effective pulse number) for producing a surface covered with closely packed dome structures. While for 100 pulses (see Figure 2(a)) only few domes can be appreciated, for $N_{eff} \geq$ 200 pulses (see Figure 2(b–f)), the entire surface is covered with

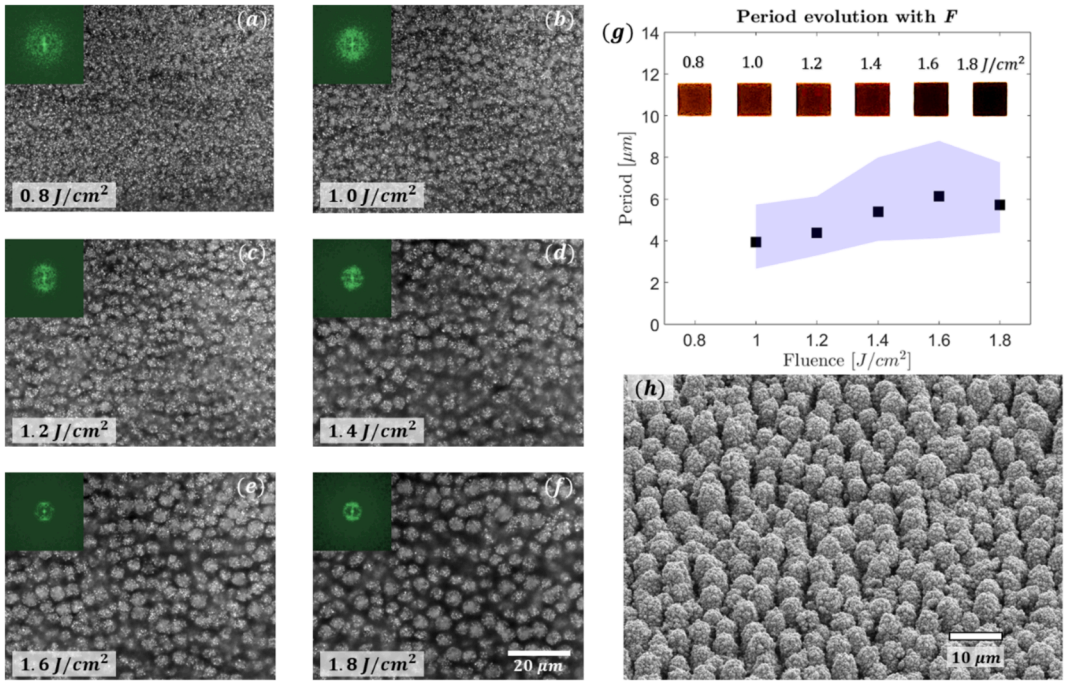

Figure 1. (a–f) OM of the areas processed at different fluences F (given as labels in each image) and constant N_{eff} = 200 pulses and f_{rep} = 50 kHz. The insets correspond to the FFT of the OM-images. (g) Evolution of the structure period with laser fluence determined from the FFTs. Symbols and shaded area correspond respectively to the obtained main period and periodicity range (see Section 2). On top of the data points, a strongly contrast-enhanced colour photograph of the 6 dark processed areas on bare Si upon specular illumination is included. (h) 45° SEM image of the region processed at F = 1.4 J/cm^2, featuring dome-like structures.

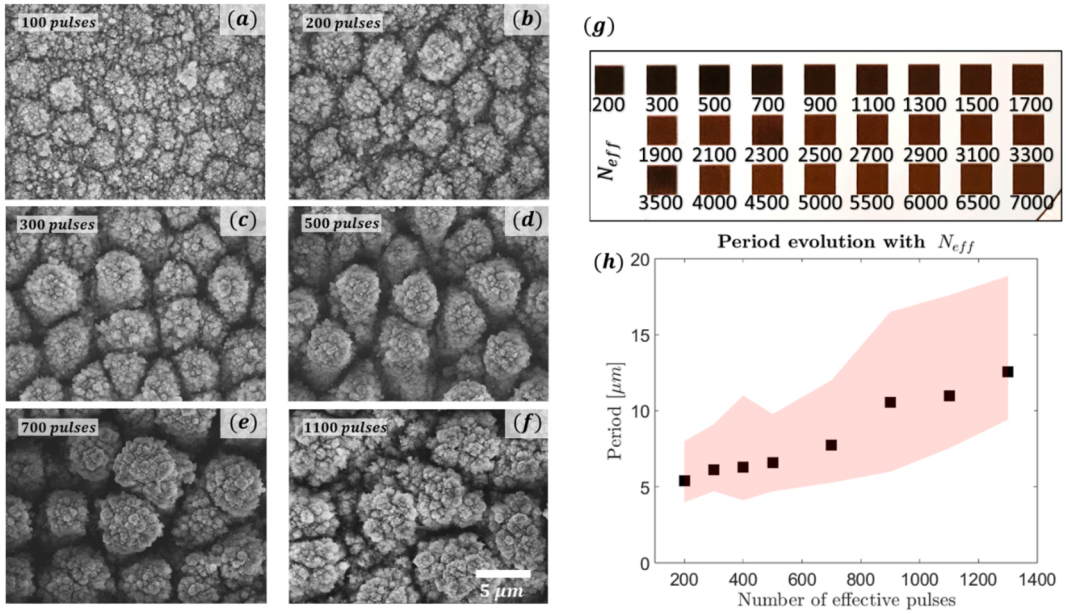

Figure 2. (a-f) Top-view SEM images of the processed areas for different N_{eff} values (F = 1.4 J/cm^2, f_{rep}= 50 kHz), below the N_{eff} threshold for formation of periodical structures (a) and above the threshold (b-f). The corresponding N_{eff} values are indicated as labels. (g) Contrast-enhanced colour photograph of the processed wafer regions on bare Si upon specular illumination. (h) Evolution of the cone period as a function of the number of effective pulses. Symbols correspond to obtained period values and shaded area indicate the periodicity range.

particle-decorated domes. Although these top-view SEM do not provide a quantitative height information, the shadows around the domes indicate a considerable evolution in the dome height with pulse number, evolving from rather flat domes into micropillars. The structures formed for N_{eff} = 200, (same as in Figure 1(d) and 1(h)), 300 and 500 pulses appear similar in terms of diameter and separation, but appear to have considerable differences in height. This means that the pillar height increases with the number of pulses, which is consistent with previous reports [8,10,14,33]. When even more pulses are used, the diameter of the domes begins to increase (see Figure 2(e) for N_{eff} = 700) and so does the diameter of the nanoparticle that form the cone decoration, until the structures obtain a blackberry-like appearance, as can be seen in Figure 2(f) for N_{eff} = 1100 pulses.

In Figure 2(g), a contrast-enhanced colour photograph of the wafer

region that contains all processed areas is shown upon specular illumination of the wafer with respect to the camera. For $N_{eff} \geq 1300$, the colour of the area turns more and more brown for increasing pulse numbers, which indicates that less visible light is absorbed. This behaviour might be related to the fact that both the cone diameter and the decorating nanoparticle size are further increasing, which seems not to be beneficial for reduction of reflectivity.

Figure 2(h) displays the evolution of the dome period with N_{eff}, determined from performing FFTs on the OM images recorded from these samples (OM images not shown) for the lower range of pulse numbers that have a dark appearance. The period increases from $\Lambda = 5.2$ µm at $N_{eff} = 200$ pulses to $\Lambda = 12.6$ µm at $N_{eff} = 1300$ pulses. For much higher N_{eff} values ($N_{eff} > 1300$), the much larger pillars formed are less and less ordered and it is not possible to determine reliable values for the period (see Supplementary Figure S4).

In order to explore the impact of the pulse number on reflectivity and transmission, we have performed a single-location (static) multi-pulse study, keeping constant $F = 1.4$ J/cm^2. For this purpose, static laser processing has been performed in order to fabricate multiple spots with different pulse numbers. It should be noted that in this study the number of pulses per irradiation spot, N, instead of the number of effective pulses, N_{eff}, will be investigated since the pulse overlap is 100%. We have used the lowest f_{rep} of this work (10 kHz), in order to achieve a precise control of the number of shots reaching each spot, using the available trigger options. The results of this study are included in Figure 3, where a selection of SEM images for different N-values is shown. For $N = 5$, horizontal ripples appear with a periodicity close to the laser wavelength, which is consistent with the formation of so-called low spatial frequency LIPSS [12]. As N is increased up to $N = 50$, these ripples are progressively substituted by randomly oriented drop-like structures that increase in size and separation. For $N = 100$ and higher pulse numbers, the space between drop-like structures appears dark, which is indicative of a depth increase and progressive transformation into pillar-like structures. Although no analysis of a possible periodicity of these structures can be made because of their low number, the pillar separation appears to increase with pulse number, in agreement with the area-processing results shown in Figure 2.

In order to further investigate the role of N and the induced morphologies that can be seen in the SEM images on the optical performance, the transmission in the center of each irradiation spot at a wavelength of 1064 nm has been measured with a low power cw laser (see Figure 3(right)). The plot shows a sudden strong decrease of transmission already at low pulse numbers ($T = 0.11$ for $N = 10$), where no spikes have formed. As can be seen from the SEM images, the spike formation threshold lies much higher, between $N = 100$ and $N = 200$ (see also Figure 2). Yet, the transmission does not decrease not much more ($T = 0.07$ for $N = 100$). This suggests that the effect of spike formation mainly contributes to a decrease in reflectivity, which is confirmed looking at the OM images of the spots recorded (insets of the transmission plot in Figure 3), showing a darkening for $N = 10$ and a virtually black appearance for $N = 300$. The complete series of the OM images for different pulse numbers is provided in the Supplementary information.

As stated before, we are interested in producing tall and closely packed structures in order to reduce the reflectivity of the processed samples [45], which means that an elevated number of pulses is required. On the other hand, as we aim for developing a cost-effective processing method, which requires that the processing time should not be too long. For these reasons, and putting together the results shown for the N_{eff} and N studies, we have chosen to continue working with $N_{eff} = 700$ pulses as a fixed parameter for the following study that explores the f_{rep}-dependence, because of the features of the morphologies achieved for this number of pulses (pillar-shaped microstructures with low reflectivity and transmittance).

The motivation for exploring the influence of the repetition rate is related to the different heat accumulation that can be expected. For the present case of Si and fs laser irradiation at a wavelength of 1030 nm, the deposition of the laser energy occurs via non-linear absorption. Once the energy is deposited in the electron system, it relaxes to the lattice via electron-phonon coupling and conventional heat diffusion takes place, reducing the surface temperature. The speed of this cooling process strongly depends on the thermal conductivity of the material, which is high for Si. Even though, for irradiation with a train of pulses at high repetition rates, a situation might arise in which the material does not have sufficient time to cool down completely before the next laser pulses. In such situation, a progressive increase of the base temperature of the material occurs and consequently an increase of the peak temperatures, which inevitably will lead to differences in the final structures produced.

The result of the f_{rep} study is shown in Figure 4. Six different f_{rep} values have been explored with the fixed conditions of $F = 1.4$ J/cm^2 and $N_{eff} = 700$, fabricating large areas. We have performed cross section SEM analysis of the samples (obtained by cleaving through the area centre), in order to determine the aspect ratio of the achieved structures before choosing the best candidates for spectrophotometry. The lowest repetition rate used was 50 kHz (see Figure 4(a)), which has been fabricated using the same processing conditions as the sample shown in Figure 2(e). The observed morphology for this case is more pillar-shaped (similar size for summit and base of the structures) than spike-shaped, and the structures are taller than the dome structures expected for lower pulse numbers. Moreover, the structures are decorated with larger

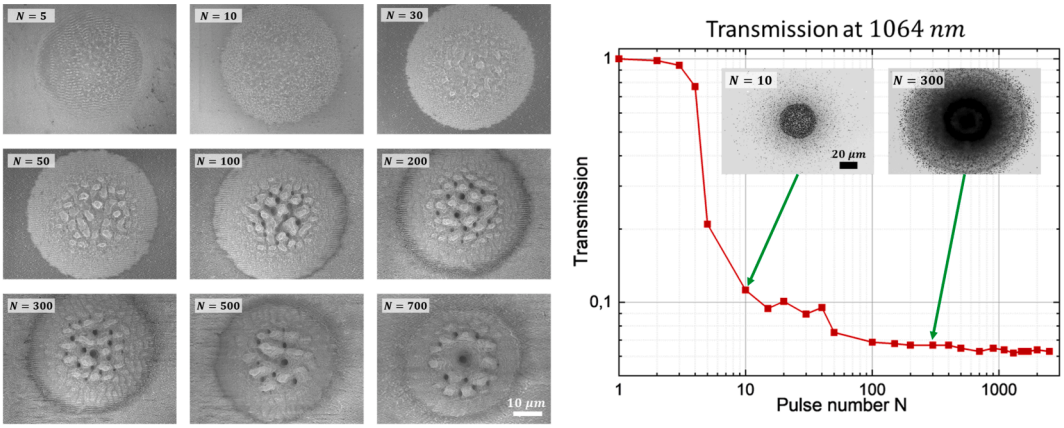

Figure 3. (left) SEM images of the irradiations performed at single locations for different pulse numbers N and constant $F = 1.4$ J/cm^2 and $f_{rep} = 10$ kHz. (right) Plot of the normalized transmission of a 1064 nm probe laser incident at the center of each area as a function of N. The insets correspond to OM images of selected spots at $N = 10$ and $N = 300$.

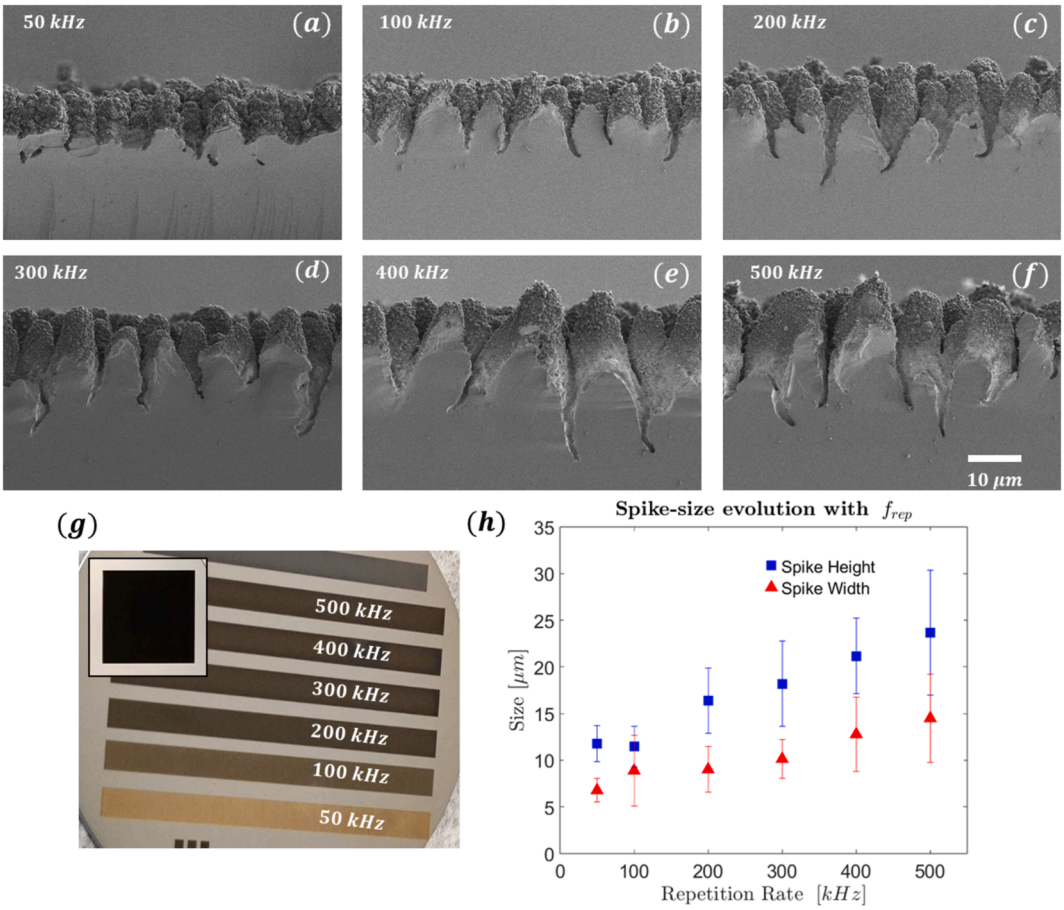

Figure 4. (a-f) Cross section SEM images of areas processed at different repetition rates (50 to 500 kHz, $F = 1.4$ J/cm^2, $N_{eff} = 700$ pulses). (g) Colour photograph of the processed wafer upon non-specular illumination to enhance the visibility of the dark areas via diffuse light scattering. The inset shows a 300 kHz area upon specular illumination to emphasize its black coloration in contrast to the bright silicon background. (h) Evolution of the average height and width of the fabricated spikes determined from the SEM images. The statistical deviation is displayed as error bars.

particles, most likely as a result of material redeposition [46,47], that may be involved in the generation of periodic structures on silicon [48,49]. When f_{rep} is increased, the surface morphology quickly becomes more conical/spike-like. The shape of the structures obtained at 100 kHz (Figure 4(b)) is more similar to that of the spikes found in BSi produced upon fs-processing in SF_6 [10,15,24,29,31–33,38]. However, at this repetition rate, the spike height is still relatively small. Upon further increasing the repetition rate up to 500 kHz (see respectively Figure 4(c) to Figure 3(f)) the shape of the structures evolves towards a distinctive conical spike-shape with an increased height. These morphological changes are beneficial for triggering multiple reflection processes of incident photons, thus enhancing light absorption [16,33,37,45]. This improved absorption for higher repetition rates can be appreciated in Figure 4(g), which shows a photograph upon non-specular illumination of the wafer before cleaving. The advantage of non-specular illumination to assess the reflection properties is that more scattered light reaches the camera and allows a finer differentiation of small changes in reflectivity. For comparison, the inset in Figure 4(g) shows a square area processed at 300 kHz upon specular illumination, confirming its deep black appearance. The areas processed at 300-500 kHz are much darker than those processed at lower values of f_{rep}, demonstrating a much lower reflectivity at least for the visible region.

The spike height (h) and width (w) of the fabricated structures have been determined from a series of cross section SEM images with a 4 times larger field of view (300 μm wide) in order to obtain reliable statistics (see Supplementary Figure S6). The results are displayed in Figure 4(h), confirming in a quantitative way the previously discussed morphological evolution: as f_{rep} is increased, the spike height and spike width also increase. In particular, the results reveal a nearly linear increase in the mean height value from $h = 12$ μm to 22 μm for the studied repetition rate range. For comparison, the mean value of the width increases from $w = 6$ μm to 14 μm. The large size of the error bars is due to the variety of structures, in particular for the highest f_{rep} values. As we are interested in achieving tall structures densely covering the surface of the material [45], we have calculated the aspect ratio (h/w) for all repetition rates (see Supplementary Figure S7), showing that the highest h/w values are obtained for 200 and 300 kHz.

We attribute the observed increase in the spike height and width with repetition rate to the increase in the base temperature described above, as a consequence of heat accumulation. The higher base temperature upon arrival of the next pulse leads to higher peak temperatures and therefore more efficient ablation, which is consistent with the deeper spikes we observe experimentally. Other works have investigated the effect of heat accumulation in silicon in air in the regime of ripple and spike formation [36,49,50]. Allahyari et al. [50] report significant differences in terms of surface morphology and crater size (no area scanning) for repetition rates > 10 kHz. Hu et al. [49] report similar results and propose plume shielding as possible mechanism to increase fluence thresholds. Our results do not indicate the presence of significant plume shielding but demonstrate the opposite effect, more efficient processing due to heat accumulation. This conclusion is also supported by the increase of the spike width, being proportional and near-equal to the spike period, with repetition rate. Following the above interpretation of a heat accumulation-induced temperature rise, the effect is

similar to increasing the fluence, which leads to an increase in period (see Figure 1).

While the two works discussed above are limited to single point irradiations, Nava et al. [36] report area processing studies and show results of surface morphology and light absorption. In their work, the authors demonstrate similarly high absorption as our results but for a narrower spectral range ($A > 94\%$ for 350 nm-1000 nm) for repetition rates up to 1 MHz via individual fine tuning of the parameters. Moreover, they introduce a so-called figure of merit, which is essentially the accumulated fluence $F_{acc} = F{\cdot}N_{eff}$, being the product of peak fluence and number of pulses. We have taken up this idea and applied it to our results by combining the data of the spike period of Figure 1 and Figure 2 as a function of F_{acc}, leading to the evolution plotted in Figure 5.

The results show a systematic, continuous increase of the spike period with F_{acc}, with data points densely covering the wide fluence window. Although the statistical error is apparently large due to the method of the periodicity range determination explained in the Supplementary information, the data points themselves show very little fluctuations along this evolution, despite the very different processing conditions in terms of pulse number and peak fluence. The related data of figure of merit shown in [36] show a slightly different evolution with a single slope, although they present considerably more scatter and are sparsely distributed.

The figure also includes the data set from Figure 4 (f_{rep} study), providing data at a constant value of F_{acc}. Although the plotted values (open circles) in this case are not the periods but the base widths of the structures determined from SEM cross sections, both parameters are expected to be similar. This is demonstrated by the fact that the lowest width(period)-value of this data set is comparable to the period-value from Figure 2(h) at the same accumulated fluence, well within the periodicity range. The strong increase of the period with repetition rate at constant F_{acc} for the data from Figure 4 points out the enormous potential of this additional parameter to further extend the range of achievable periods. The combined tuning range of the spike period for the single wavelength used (1030 nm), employing accumulated fluence and repetition rate, is 4 μm – 14 μm. Moreover, the plot indicates that longer periods might be possible by combining high repetition rates and high accumulated fluences.

As a next step, we have fabricated several macroscopic areas ($1.1{\times}1.1$ cm^2) using the optimized processing conditions identified in the previous three steps for fabricating spike-like structures with elevated heights and low reflectivity in the visible. According to the above results, these conditions are $F = 1.4$ J/cm^2, $N_{eff} = 700$ pulses and

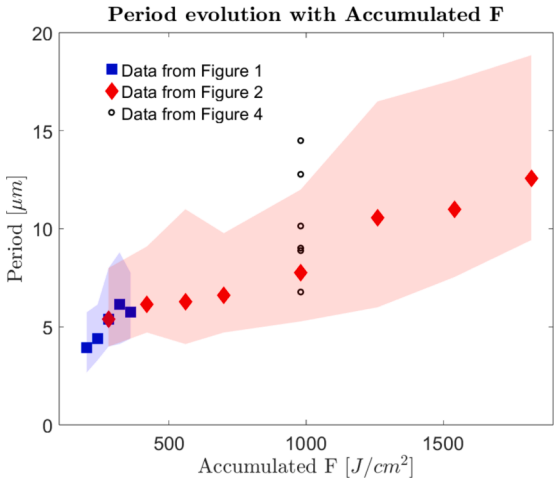

Figure 5. Evolution of the microstructures period with the accumulated fluence ($F_{acc} = F{\cdot}N_{eff}$). The data for this graphic has been generated from the data of Figure 1 (blue squares), Figure 2 (red diamonds) and Figure 4 (black open circles).

$f_{rep} \geq 200$ kHz, leading to an aspect ratio of $\approx 1.8{\pm}0.6$ (height/width) for 300 kHz. Performing measurements of the samples absorptance with the spectrophotometer, we observed noticeable local differences and reproducibility issues for the repetition rates 400 kHz and 500 kHz, which we attribute to the increasing thermal load. In turn, for the structures fabricated at 300 kHz, the obtained absorption spectra measured for several samples fabricated under the same conditions were highly reproducible, which is why we have chosen $f_{rep} = 300$ kHz as the optimal repetition rate for producing SSi.

The measured absorption spectra are shown in Figure 6(a). In the discussion of the results we will make a distinction between the range $\lambda < 1100$ nm, where pristine Si absorbs light, and $\lambda > 1100$ nm, where it is transparent; the bandgap being $E_{g,Si} = 1.12$ eV $\Rightarrow \lambda_{g,Si} = 1100$ nm. As anticipated by the black colour upon visual inspection, fs-processing (red curve) has led to a strong improvement of the semiconductor's absorptance in the VIS-NIR region, raising from a maximum value of $A = 68\%$ for pristine Si to a spectrally rather constant value of $A = 95\%$ for fs-processed Si. Noteworthy, this improvement includes the ultraviolet (UV) part of the spectrum which performs rather poor for pristine Si. The achieved increase in light absorption can be directly related to the texturing and the multiple reflection phenomenon that dominates the light interaction process with the material [13–15]. On the other hand, a strong enhancement of the MIR absorption is observed for $\lambda > 1100$ nm, which decays progressively to a value of $A = 26\%$ at 2500 nm. Contrary to the case of hyperdoped BSi processed in SF_6 gas [15,19,24,31–33], where the IR absorptance is mainly due to the incorporation of the S-atoms in the Si lattice, here the sub-bandgap absorption is likely related to defects and lack of crystallinity induced by the fs-processing, since no dopants are incorporated in the Si lattice except a possible incorporation of nitrogen or oxygen from the air atmosphere [37]. In order to eliminate the part due to the poor crystalline quality, PLA and RTA treatments have been performed. In Figure 6(b), the Raman spectra of the fs laser processed samples treated with the two annealing techniques are compared to those of the pristine and as-processed Si. As observed, the Raman intensity signal from the characteristic Raman bands of amorphous Si (transversal acoustic Raman mode, TA, at 150 cm^{-1} and transversal optic Raman mode, TO, at 480 cm^{-1}[51]) is clearly visible in the as-processed material but is strongly suppressed after PLA and RTA treatments, making the spectra closer to that of the pristine material, indicating an effective recrystallization-induced process. Nonetheless, the asymmetric broadening of the peak centered at 520 cm^{-1} indicates either recrystallization into the polycrystalline phase or a contribution from a small remaining amorphous phase.

Also, changes in absorption for both annealing procedures can be seen in Figure 6(a), with some differences between them. For the PLA case, there is a small absorption reduction for $\lambda > 1100$ nm with respect to the as-processed sample, but accompanied by a slight improvement in absorption (up to ~97%) for 400 nm $\leq \lambda \leq$ 850 nm. For RTA, a strong reduction of absorptance is observed for $\lambda > 1100$ nm, to a constant value of $A = 22\%$ between 1200-2500 nm, while preserving an $A > 94\%$ in the UV-VIS region. Comparing the Spectrophotometry and Raman results for the annealed samples, it is possible to derive complementary information: for the PLA case, the Raman measurements reveal near-complete superficial recovery of crystallinity, whereas the barely reduced absorption in the MIR region can be interpreted as a sign of the deep lying defects and impurities acting as intermediate energy levels in the semiconductor's gap, triggering the absorption of MIR photons. In this respect, the EDX measurements show a strong increase of the oxygen content upon laser processing (from ~1 at% for the pristine material to ~30 at% for as-processed SSi, as can be seen in Table 1) while nitrogen incorporation can be considered as negligible. Although these results may be somewhat conditioned by the topography of the sample, similar results have been observed in ref. [31] in samples irradiated in air and N_2, employing a different composition sensitive technique. There, oxygen incorporation was attributed to the formation of a silicon rich sub-stoichiometric silicon oxide layer. According to our results, part

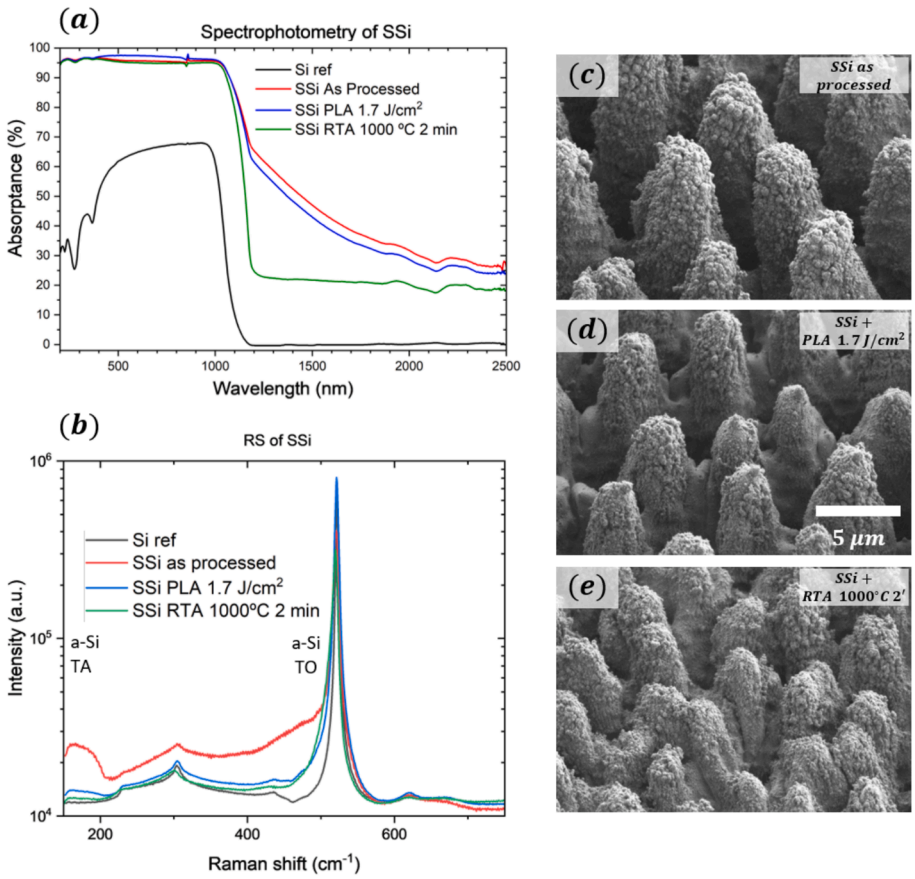

Figure 6. (a) Absorptance spectra measured in the range from 250 to 2500 nm by spectrophotometry for samples processed at $F = 1.4$ J/cm^2, $N_{eff} = 700$ pulses and $f_{rep} = 300$ kHz for different postprocessing steps: as fabricated (red curve), annealed by excimer irradiation at 1.7 J/cm^2 (blue curve), annealed by rapid thermal annealing at 1000°C for 2 minutes (green curve) compared to a pristine monocrystalline wafer of (100)-Si (black curve) . (b) Raman spectroscopy performed for the same materials as in (a), indicating the spectral positions of the two dominant modes of amorphous Si (c-e) SEM images at 45° angle of the as-processed sample (c), annealed by excimer laser irradiation (PLA) at $F_{PLA} = 1.7$ J/cm^2 (d) and by rapid thermal annealing (RTA) (e).

Table 1
EDX quantification of the amount of Si, O and N present in three different samples: a pristine silicon surface, a SSi surface (processed at $F = 1.4$ J/cm^2, $N_{eff} = 700$ pulses and $f_{rep} = 500$ kHz) and a SSi after a RTA treatment at 1000 °C for 2 minutes. The measurement resolution is ~1 at%.

Quantified Element	Pristine Si Surface	SSi as-processed	SSi + RTA
Si	99 at%	69 at%	75 at%
O	1 at%	31 at%	25 at%
N	Below resolution	Below resolution	Below resolution

of this layer decomposes during RTA to yield ~24 at% oxygen content. The contribution to the absorption of this remnant oxygen, incorporated in the material, must be though small, consistently with the MIR absorption behaviour. The RTA sample does not show a decaying absorption in the MIR-IR region which supports that the defects associated to the oxygen incorporation are effectively annealed upon RTA. It anneals the entire wafer thickness, including deep lying defects as opposed to PLA, that only affects a shallow surface layer. The constant value of MIR sub-bandgap absorption after RTA post-processing can be attributed to the geometry of the spike structure, enhancing the coupling and trapping of incident light [13].

The morphological appearance of the microstructures is shown in Figure 6(c-e). Compared to the as-processed samples shown in Figure 6 (c), the structures after PLA post-processing (see Figure 6(d)) are shorter and less sharp. In the case of the RTA post-processed sample shown in Figure 6(e), the structures are even shorter, reducing the aspect ratio of the spikes. Yet the excellent performance in absorption of the annealed samples (Figure 6(a)) demonstrates that this reduction of the height and aspect ratio does not compromise the optical performance.

Due to the positive effect of the RTA treatment in the crystalline quality of the SSi samples, we have performed an electrical characterization (see Section 2) to compare a bare-Si sample, an as-processed SSi sample and a rapid thermally annealed SSi piece. Table 2 shows the

Table 2
Electrical characterization of a bare-Si sample, an as processed SSi and a SSi + RTA (1000 °C for 2 minutes). The mean values of sheet resistance, mobility and carrier density (n) of the tow samples are indicated with their corresponding error, calculated as the statistical deviation of the measurements.

	Bare Si		SSi as processed		SSi + RTA	
Sheet Resistance [Ω/sq]	164.91	± 0.17%	172.10	± 1.47%	163.62	± 1.40%
Mobility [$cm^2/(s{\cdot}V)$]	348.81	± 0.71%	317.32	± 1.48%	349.67	± 0.78%
n[$\times 10^{15} cm^{-3}$]	2.17	± 0.69%	2.29	± 0.22%	2.18	± 1.26%

sheet resistance obtained with the van der Pauw configuration, the Hall mobility and carrier concentration measured with the Hall effect for these samples.

Mobility is the measured electrical parameter that is more related to the possible lack of crystallinity. The mobility of the as processed SSi sample decreases compared with the Si crystalline substrate (around a 9%), suggesting that after the laser microstructuring process, the degree of crystallinity in the surface has decreased (which is supported by the Raman spectra shown in Figure 6). The difference found in the mobility values cannot be attributed to a difference in the measurement, since the typical deviation between consecutive measurements in the same sample is clearly lower than between the mentioned two different samples. However, after the RTA treatment, the microstructured Si sample shows a similar value than the crystalline reference, pointing out a lattice damage recovery, which agrees with the previous discussion for the RS and Spectrophotometry analysis (see Figure 6). Furthermore, sheet resistance is inversely proportional to the product of mobility and the carrier concentration majority type. The sheet resistance measurements after fs-laser processing are higher than the Si crystalline reference, in agreement with the lower mobility observed. After the RTA process, the sheet resistance is similar to the substrate, in agreement with the recovery of the mobility.

Considering the electrical characterization results, the behaviour of the processed and annealed sample is as good as in the case of the pristine material, without any laser processing, contrary to the case of the sample fs-processed without annealing treatment. Since the van der Pauw technique is only valid for homogeneous flat surfaces, in the samples with spikes, we are measuring the substrate, being negligible the contribution of the spikes to the electrical properties. Then, we suggest that we are removing defects (increasing the Hall mobility) in the surface just below the spikes. These defects might have been created during the spike fabrication process, as is supported by the previous discussion. The reduction of the carrier concentration for the sample RTA processed points also to this hypothesis, and the removed defects could have electrical activation at RT for the as-processed sample. Together with the RS, Spectrophotometry and EDX microanalysis shown in Figure 6 and Table 1, these electrical measurements support RTA as a fundamental part of the semiconductor functionalization, because allows the annealing of defects and amorphous phases induced during the fs-laser processing, allowing the use of the presented SSi for future applications in the field of optoelectronics and photovoltaics.

4. Conclusions

In this study, a fs-laser processing approach in ambient air is proposed in order to improve light absorption in Si without hyperdoping the material, while avoiding the use of greenhouse gases during the texturing. We have explored and analysed in detail the influence of the three main processing parameters (laser fluence F, pulse number N_{eff} and pulse repetition rate f_{rep}) on the formation of black non-hyperdoped silicon (spiky silicon). As a global result, we observe that the period of the structures can be tuned by any of these three parameters, being able to increase it from ~4 μm to ~14 μm by increasing the accumulated fluence and/or the repetition rate. Moreover, the influence of N_{eff} on the surface morphology is vital for enhancing light trapping, as a high pulse number leads to taller pillars (essential for multiple reflection processes to happen). Finally, the impact of f_{rep} is equally important since an increase triggers a rise of the base temperature of the sample by heat accumulation, which yields a more efficient ablation that leads to an increase of depth and period of the spikes. We have identified as optimum processing conditions $F = 1.4$ J/cm^2, $N_{eff} = 700$ pulses, $f_{rep} = 300$ kHz for obtaining highly reproducible black spiky textures in silicon. The scalability of the processing is possible due to its relatively short processing times, around 127 seconds for a 1 cm^2 area.

In terms of optical performance, the processed material shows an absorption $A > 94\%$ in the range 250-1100 nm. Raman spectra show that crystallinity of the material can be recovered almost completely with both PLA and RTA treatments, but deep defects can only be removed by RTA (shown by optical and electrical measurements), which is important for optoelectronic applications where carrier mobility is essential. The absorptance of the thermally annealed recrystallized material remains $> 94\%$ and its sheet resistance, mobility and carrier density are equally good as non-processed silicon, which suggests this material to be an excellent candidate for technologies requiring efficient use of light, as light sensing or photovoltaics. Furthermore, for $\lambda > 1200$ nm, the absorption remains above 20% without doping, which suggest its possible use in IR technology.

As an outlook for follow-up strategies, we would like to mention hyperdoping of the annealed spike structures, avoiding the use of greenhouse gases during both the texturing and the hyperdoping, in order to improve the absorption in the MIR-region. Also, the influence of several other irradiation parameters deserves attention, such as the laser wavelength, ambient gas conditions (processing atmosphere and atmosphere pressure), as well as highest repetition rates, aimed at annealing the surface during processing and possibly extending the tuning range. We expect that such additional strategies will further improve the material performance and enable implementation of SSi in PV, such as solar cells or photodetectors, and also in other fields where other functionalities of these structures are exploited, such as wettability, biosensing or cell adhesion.

CRediT authorship contribution statement

Gonzalo Gomez-Munoz: Writing – original draft, Visualization, Methodology, Investigation, Formal analysis, Data curation. **Rafael Benítez-Fernández:** Writing – review & editing, Investigation, Funding acquisition, Data curation. **Guillermo Godoy-Perez:** Funding acquisition, Data curation. **Fatima Cabello:** Writing – review & editing, Investigation, Data curation. **Marina Garcia-Pardo:** Investigation, Data curation. **Daniel Caudevilla:** Writing – review & editing, Investigation, Data curation. **Jose Gonzalo:** Writing – review & editing, Resources, Methodology, Investigation, Data curation. **Javier Solis:** Writing – review & editing, Resources, Funding acquisition. **Mario Garcia-Lechuga:** Writing – review & editing, Investigation, Funding acquisition. **Javier Olea:** Writing – review & editing, Resources, Funding acquisition. **David Pastor:** Writing – review & editing, Supervision, Resources, Project administration, Methodology, Investigation, Funding acquisition, Conceptualization. **Jan Siegel:** Writing – review & editing, Validation, Supervision, Resources, Project administration, Methodology, Investigation, Funding acquisition, Data curation, Conceptualization.

Declaration of competing interest

The authors declare that they have no known competing financial interests or personal relationships that could have appeared to influence the work reported in this paper.

Acknowledgements

This work has been supported by grant HyperSolar (TED2021-130894B-C21 and TED2021-130894B-C22) funded by MICIU/AEI/10.13039/501100011033 and by the "European Union NextGenerationEU/PRTR", grant ULS_PSB (PID2020-112770RB-C21) funded by MICIU/AEI/10.13039/501100011033, and grant HyperPHIR (PID2020-117498RB-I00) funded by the Spanish Research Agency (AEI, Ministry of Research and Innovation), the European Regional Development Fund (ERDF) and by the Spanish Ministry of Science and Innovation. G. Godoy-Pérez and R. Benítez-Fernández acknowledge the research contracts under the Investigo Program (CT19/23-INVM-35 and CT19/23-INVM-27) of the Ministerio de Trabajo y Economía Social. The

authors would like to thank David Gomez at ICTP-CSIC for performing the 45° SEM measurements. Authors want to acknowledge assistance from CAI de Técnicas Químicas (Espectroscopía Raman y Correlación) and CAI de Técnicas Físicas (Implantación Iónica) from the Universidad Complutense de Madrid for Raman measurements and RTA. We also acknowledge ICTS-CNME (Madrid, Spain) for the SEM images and EDX characterization.

Appendix A. Supplementary material

Supplementary data to this article can be found online at https://doi.org/10.1016/j.apsusc.2024.161967.

Data availability

The authors do not have permission to share data.

References:

[1] M. Mezera, C. Florian, G. Römer, J. Krüger, J. Bonse, Creation of Material Functions by Nanostructuring, in: R. Stoian, J. Bonse (Eds.), Ultrafast Laser Nanostructuring, Springer Series in Optical Science, Springer, Cham, 2023, pp. 827–886, https://doi.org/10.1007/978-3-031-14752-4_23.
[2] E. Stratakis, J. Bonse, J. Heitz, J. Siegel, G.D. Tsibidis, E. Skoulas, A. Papadopoulos, A. Mimidis, A.-C. Joel, P. Comanns, J. Krüger, C. Florian, Y. Fuentes-Edfuf, J. Solis, W. Baumgartner, Laser engineering of biomimetic surfaces, Mater. Sci. Eng. R. Rep. 141 (2020) 100562, https://doi.org/10.1016/j.mser.2020.100562.
[3] A.Y. Vorobyev, C. Guo, Direct femtosecond laser surface nano/microstructuring and its applications, Laser Photon Rev 7 (2013) 385–407, https://doi.org/10.1002/lpor.201200017.
[4] J. Bonse, A. Rosenfeld, J. Krüger, On the role of surface plasmon polaritons in the formation of laser-induced periodic surface structures upon irradiation of silicon by femtosecond-laser pulses, J. Appl. Phys. 106 (2009), https://doi.org/10.1063/1.3261734.
[5] Y. Fuentes-Edfuf, J.A. Sánchez-Gil, C. Florian, V. Giannini, J. Solis, J. Siegel, Surface plasmon polaritons on rough metal surfaces: role in the formation of laser-induced periodic surface structures, ACS Omega 4 (2019) 6939–6946, https://doi.org/10.1021/acsomega.9b00546.
[6] H. Zhang, J.-P. Colombier, C. Li, N. Faure, G. Cheng, R. Stoian, Coherence in ultrafast laser-induced periodic surface structures, PhysRevB 92 (2015) 174109, https://doi.org/10.1103/PhysRevB.92.174109.
[7] U. Hermens, S.V. Kirner, C. Emonts, P. Comanns, E. Skoulas, A. Mimidis, H. Mescheder, K. Winands, J. Krüger, E. Stratakis, J. Bonse, Mimicking lizard-like surface structures upon ultrashort laser pulse irradiation of inorganic materials, Appl. Surf. Sci. 418 (2017) 499–507, https://doi.org/10.1016/j.apsusc.2016.12.112.
[8] B.K. Nayak, M.C. Gupta, Self-organized micro/nano structures in metal surfaces by ultrafast laser irradiation, Opt. Lasers Eng. 48 (2010) 940–949, https://doi.org/10.1016/j.optlaseng.2010.04.010.
[9] P. Fan, H. Wu, M. Zhong, H. Zhang, B. Bai, G. Jin, Large-scale cauliflower-shaped hierarchical copper nanostructures for efficient photothermal conversion, Nanoscale 8 (2016) 14617–14624, https://doi.org/10.1039/c6nr03662g.
[10] B.R. Tull, J.E. Carey, E. Mazur, J.P. McDonald, S.M. Yalisove, Silicon surface morphologies after femtosecond laser irradiation, MRS Bull 31 (2006) 626–633, https://doi.org/10.1557/mrs2006.160.
[11] C. Florian Baron, A. Mimidis, D. Puerto, E. Skoulas, E. Stratakis, J. Solis, J. Siegel, Biomimetic surface structures in steel fabricated with femtosecond laser pulses: influence of laser rescanning on morphology and wettability, Beilst. J. Nanotechnol. 9 (2018) 2802–2812, https://doi.org/10.3762/bjnano.9.262.
[12] G.D. Tsibidis, C. Fotakis, E. Stratakis, From ripples to spikes: A hydrodynamical mechanism to interpret femtosecond laser-induced self-assembled structures, PhysRevB 92 (2015) 041405, https://doi.org/10.1103/PhysRevB.92.041405.
[13] P. Campbell, M.A. Green, Light trapping properties of pyramidally textured surfaces, J. Appl. Phys. 62 (1987) 243–249, https://doi.org/10.1063/1.339189.
[14] V.V. Iyengar, B.K. Nayak, M.C. Gupta, Optical properties of silicon light trapping structures for photovoltaics, Sol. Energy Mater. Sol. Cells 94 (2010) 2251–2257, https://doi.org/10.1016/j.solmat.2010.07.020.
[15] B. Franta, E. Mazur, S.K. Sundaram, Ultrafast laser processing of silicon for photovoltaics, Int. Mater. Rev. 63 (2018) 227–240, https://doi.org/10.1080/09506608.2017.1389547.
[16] X. Zhao, K. Lin, B. Zhao, W. Du, J.J.J. Nivas, S. Amoruso, X. Wang, Broadband MSM photodetector based on S-doped black silicon fabricated by femtosecond laser, Appl. Surf. Sci. 619 (2023) 156624, https://doi.org/10.1016/j.apsusc.2023.156624.
[17] Y. Borodaenko, S. Syubaev, S. Gurbatov, A. Zhizhchenko, A. Porfirev, S. Khonina, E. Mitsai, A.V. Gerasimenko, A. Shevlyagin, E. Modin, S. Juodkazis, E.L. Gurevich, A.A. Kuchmizhak, Deep subwavelength laser-induced periodic surface structures on silicon as a novel multifunctional biosensing platform, ACS Appl. Mater. Interf. 13 (2021) 54551–54560, https://doi.org/10.1021/acsami.1c16249.
[18] M.J. Smith, Y.-T. Lin, M.-J. Sher, M.T. Winkler, E. Mazur, S. Gradečak, Pressure-induced phase transformations during femtosecond-laser doping of silicon, J. Appl. Phys. 110 (2011), https://doi.org/10.1063/1.3633528.
[19] Z. Tong, M. Bu, Y. Zhang, D. Yang, X. Pi, Hyperdoped silicon: Processing, properties, and devices, J. Semicond. 43 (2022) 093101, https://doi.org/10.1088/1674-4926/43/9/093101.
[20] M.J. Smith, M.-J. Sher, B. Franta, Y.-T. Lin, E. Mazur, S. Gradečak, Improving dopant incorporation during femtosecond-laser doping of Si with a Se thin-film dopant precursor, Appl. Phys. A 114 (2014) 1009–1016, https://doi.org/10.1007/s00339-013-7673-8.
[21] Y. Fuentes-Edfuf, M. Garcia-Lechuga, D. Puerto, C. Florian, A. Garcia-Leis, S. Sanchez-Cortes, J. Solis, J. Siegel, Fabrication of amorphous micro-ring arrays in crystalline silicon using ultrashort laser pulses, Appl. Phys. Lett. 110 (2017), https://doi.org/10.1063/1.4984110.
[22] M.-J. Sher, E.G. Hemme, Hyperdoped silicon materials: from basic materials properties to sub-bandgap infrared photodetectors, Semicond. Sci. Technol. 38 (2023) 033001, https://doi.org/10.1088/1361-6641/acb16b.
[23] X. Dong, N. Li, Z. Zhu, H. Shao, X. Rong, C. Liang, H. Sun, G. Feng, L. Zhao, J. Zhuang, A nitrogen-hyperdoped silicon material formed by femtosecond laser irradiation, Appl. Phys. Lett. 104 (2014), https://doi.org/10.1063/1.4868017.
[24] B. Franta, D. Pastor, H.H. Gandhi, P.H. Rekemeyer, S. Gradečak, M.J. Aziz, E. Mazur, Simultaneous high crystallinity and sub-bandgap optical absorptance in hyperdoped black silicon using nanosecond laser annealing, J. Appl. Phys. 118 (2015), https://doi.org/10.1063/1.4937149.
[25] J.C. Zolper, S. Narayanan, S.R. Wenham, M.A. Green, 16.7% efficient, laser textured, buried contact polycrystalline silicon solar cell, Appl. Phys. Lett. 55 (1989) 2363–2365, https://doi.org/10.1063/1.102019.
[26] S. Xiao, S. Xu, High-efficiency silicon solar cells—materials and devices physics, Crit. Rev. Solid State Mater. Sci. 39 (2014) 277–317, https://doi.org/10.1080/10408436.2013.834245.
[27] M. Okil, M.S. Salem, T.M. Abdolkader, A. Shaker, From crystalline to low-cost silicon-based solar cells: a review, Silicon 14 (2022) 1895–1911, https://doi.org/10.1007/s12633-021-01032-4.
[28] Y. Borodaenko, D. Pavlov, A. Cherepakhin, E. Mitsai, A. Pilnik, S. Syubaev, S. O. Gurbatov, E. Modin, A.P. Porfirev, S.N. Khonina, A.V. Shevlyagin, E.L. Gurevich, A.A. Kuchmizhak, Liquid-assisted laser nanotexturing of silicon: onset of hydrodynamic processes regulated by laser-induced periodic surface structures, Adv. Mater. Technol. 9 (2024), https://doi.org/10.1002/admt.202301567.
[29] T.-H. Her, R.J. Finlay, C. Wu, S. Deliwala, E. Mazur, Microstructuring of silicon with femtosecond laser pulses, Appl. Phys. Lett. 73 (1998) 1673–1675, https://doi.org/10.1063/1.122241.
[30] P. Cheng, H. Wang, B. Müller, J. Müller, D. Wang, P. Schaaf, Photo-thermoelectric conversion using black silicon with enhanced light trapping performance far beyond the band edge absorption, ACS Appl. Mater. Interf. 13 (2021) 1818–1826, https://doi.org/10.1021/acsami.0c17279.
[31] R. Younkin, J.E. Carey, E. Mazur, J.A. Levinson, C.M. Friend, Infrared absorption by conical silicon microstructures made in a variety of background gases using femtosecond-laser pulses, J. Appl. Phys. 93 (2003) 2626–2629, https://doi.org/10.1063/1.1545159.
[32] S. Kontermann, T. Gimpel, A.L. Baumann, K.-M. Guenther, W. Schade, Laser processed black silicon for photovoltaic applications, Energy Procedia 27 (2012) 390–395, https://doi.org/10.1016/j.egypro.2012.07.082.
[33] Y. Peng, Y. Zhou, X. Chen, Y. Zhu, The fabrication and characteristic investigation of microstructured silicon with different spike heights, Opt. Commun. 334 (2015) 122–128, https://doi.org/10.1016/j.optcom.2014.08.034.
[34] M. Steglich, D. Lehr, S. Ratzsch, T. Käsebier, F. Schrempel, E. Kley, A. Tünnermann, An ultra-black silicon absorber, Laser Photon. Rev. 8 (2014), https://doi.org/10.1002/lpor.201300142.
[35] H. Jansen, M. de Boer, J. Burger, R. Legtenberg, M. Elwenspoek, The black silicon method II:The effect of mask material and loading on the reactive ion etching of deep silicon trenches, Microelectron. Eng. 27 (1995) 475–480, https://doi.org/10.1016/0167-9317(94)00149-O.
[36] G. Nava, R. Osellame, R. Ramponi, K.C. Vishnubhatla, Scaling of black silicon processing time by high repetition rate femtosecond lasers, Opt. Mater. Express 3 (2013) 612, https://doi.org/10.1364/OME.3.000612.
[37] Z. Wen, Z. Zhang, K. Zhang, J. Li, H. Shi, M. Li, Y. Hou, M. Xue, Z. Zhang, Large-scale wideband light-trapping black silicon textured by laser inducing assisted with laser cleaning in ambient air, Nanomaterials 12 (2022) 1772, https://doi.org/10.3390/nano12101772.
[38] C.H. Crouch, J.E. Carey, M. Shen, E. Mazur, F.Y. Génin, Infrared absorption by sulfur-doped silicon formed by femtosecond laser irradiation, Appl. Phys. A 79 (2004) 1635–1641, https://doi.org/10.1007/s00339-004-2676-0.
[39] S. Liu, J. Zhu, Y. Liu, L. Zhao, Laser induced plasma in the formation of surface-microstructured silicon, Mater. Lett. 62 (2008) 3881–3883, https://doi.org/10.1016/j.matlet.2008.05.012.
[40] M.-J. Sher, N.M. Mangan, M.J. Smith, Y.-T. Lin, S. Marbach, T.M. Schneider, S. Gradečak, M.P. Brenner, E. Mazur, Femtosecond-laser hyperdoping silicon in an SF_6 atmosphere: dopant incorporation mechanism, J. Appl. Phys. 117 (2015) 125301, https://doi.org/10.1063/1.4914520.
[41] X. Wang, W. Du, J.J.J. Nivas, B. Zhao, X. Zhao, S. Amoruso, Direct fabrication of Te-doped black Si with an enhanced photoelectric performance by femtosecond laser irradiation under water, ACS Appl. Mater. Interf. 16 (2024) 2921–2931, https://doi.org/10.1021/acsami.3c15234.
[42] J.M. Liu, Simple technique for measurements of pulsed Gaussian-beam spot sizes, Opt. Lett. 7 (1982) 196, https://doi.org/10.1364/OL.7.000196.

[43] S.M. Sze, K.K. Ng, in: Physics of Semiconductor Devices, Wiley, 2006, https://doi.org/10.1002/0470068329.
[44] T.-H. Her, R.J. Finlay, C. Wu, E. Mazur, Femtosecond laser-induced formation of spikes on silicon, Appl. Phys. A Mater. Sci. Process 70 (2000) 383–385, https://doi.org/10.1007/s003390051052.
[45] K.N. Nguyen, D. Abi-Saab, P. Basset, E. Richalot, F. Marty, D. Angelescu, Y. Leprince-Wang, T. Bourouina, Black silicon with sub-percent reflectivity: Influence of the 3D texturization geometry, IEEE, 2011, pp. 354–357, https://doi.org/10.1109/TRANSDUCERS.2011.5969470.
[46] Y. Han, S. Qu, The ripples and nanoparticles on silicon irradiated by femtosecond laser, Chem. Phys. Lett. 495 (2010) 241–244, https://doi.org/10.1016/j.cplett.2010.06.071.
[47] C.H. Crouch, J.E. Carey, J.M. Warrender, M.J. Aziz, E. Mazur, F.Y. Génin, Comparison of structure and properties of femtosecond and nanosecond laser-structured silicon, Appl. Phys. Lett. 84 (2004) 1850–1852, https://doi.org/10.1063/1.1667004.
[48] J.J.J. Nivas, Z. Song, R. Fittipaldi, A. Vecchione, R. Bruzzese, S. Amoruso, Direct ultrashort laser surface structuring of silicon in air and vacuum at 1055 nm, Appl. Surf. Sci. 417 (2017) 149–154, https://doi.org/10.1016/j.apsusc.2017.03.158.
[49] M. Hu, J.J.J. Nivas, M. Valadan, R. Fittipaldi, A. Vecchione, R. Bruzzese, C. Altucci, S. Amoruso, Ultrafast laser surface irradiation of silicon: effects of repetition rate in vacuum and air, Appl. Surf. Sci. 606 (2022) 154869, https://doi.org/10.1016/j.apsusc.2022.154869.
[50] E. Allahyari, J.J.J. Nivas, M. Valadan, R. Fittipaldi, A. Vecchione, L. Parlato, R. Bruzzese, C. Altucci, S. Amoruso, Plume shielding effects in ultrafast laser surface texturing of silicon at high repetition rate in air, Appl. Surf. Sci. 488 (2019) 128–133, https://doi.org/10.1016/j.apsusc.2019.05.219.
[51] D. Bermejo, M. Cardona, Raman scattering in pure and hydrogenated amorphous germanium and silicon, J. Non Cryst. Solids 32 (1979) 405–419, https://doi.org/10.1016/0022-3093(79)90085-1.